

Valley Phenomena in the Candidate Phase Change Material $\text{WSe}_{2(1-x)}\text{Te}_{2x}$

Sean M. Oliver^{1,2}, Joshua Young³, Sergiy Krylyuk^{4,5}, Thomas L. Reinecke⁶, Albert V. Davydov⁴, Patrick M. Vora^{1,2,*}

¹*Department of Physics and Astronomy, George Mason University, Fairfax, VA, USA*

²*Quantum Materials Center, George Mason University, Fairfax, VA, USA*

³*Department of Physics, Applied Physics and Astronomy, Binghamton University, Vestal, NY, USA*

⁴*Functional Nanostructured Materials Group, National Institute of Standards and Technology, Gaithersburg, MD, USA*

⁵*Theiss Research, La Jolla, CA, USA*

⁶*Naval Research Laboratory, Washington, DC, USA*

*Author to whom correspondence should be addressed

Email: pvora@gmu.edu

Keywords: transition metal dichalcogenide, alloy, phase transition, valley polarization, valley coherence, Raman spectroscopy, photoluminescence spectroscopy, temperature dependence, low temperature

Abstract

Alloyed transition metal dichalcogenides provide a unique opportunity for coupling band engineering and valleytronic phenomena in an atomically-thin platform. However, valley properties in alloys remain largely unexplored. We investigate the valley degree of freedom in monolayer alloys of the phase change candidate material $\text{WSe}_{2(1-x)}\text{Te}_{2x}$. Low temperature Raman measurements track the alloy-induced transition from the semiconducting 1H phase of WSe_2 to the semimetallic 1T_d phase of WTe_2 . We correlate these observations with density functional theory calculations and identify new Raman modes from 1H- WTe_2 . Photoluminescence measurements show ultra-low energy emission features that highlight the presence of significant alloy disorder arising from the large W-Te bond lengths. Interestingly, valley polarization and coherence in alloys survive at high Te compositions and are more robust against temperature than in WSe_2 . These findings illustrate the persistence of valley properties in alloys with highly dissimilar parent compounds and suggest band engineering can be utilized for valleytronic devices.

Introduction

The valley contrasting properties of monolayer semiconducting transition metal dichalcogenides (TMDs) provide the possibility of manipulating information using the valley pseudospin¹⁻⁴ in direct analogy to spintronics.⁵ Devices that employ this schema for computation, commonly referred to as valleytronics, benefit from optical or electrical manipulation of the valley index, spin-valley locking, low power consumption, and the absence of Joule heating.^{1,3} These advantages have stimulated vigorous investigations into the properties of two-dimensional (2D) semiconducting TMDs with an emphasis on exploring the optical interband selection rules that connect photon polarization to valley index.¹⁻⁴

The first studies of monolayer TMDs focused solely on the photoluminescence (PL) from molybdenum disulfide (MoS_2),^{6,7} however attention shifted to valley-dependent studies.^{8,9} Soon after, monolayer tungsten diselenide (WSe_2) was found to be a superior TMD for valleytronics, exhibiting both exciton valley polarization and valley coherence.¹⁰⁻¹⁷ Valley polarization describes the probability of an exciton created in a valley to remain there until recombination, while valley coherence quantifies the probability of an exciton to remain in a superposition state of K and K' valleys before recombining. At low temperature, the neutral exciton (X^0) in bare WSe_2 monolayers exhibits a valley polarization ranging from 40 - 70 % depending on the laser energy.^{10,12,18} The depolarization of valley excitons is believed to be governed by a combination of intervalley electron-hole exchange interactions,^{9,19} phonon-assisted intervalley scattering,^{8,20} and Coulomb screening of the exchange interaction.^{21,22} Additionally, WSe_2 holds the record for the largest degree of X^0 valley coherence in bare monolayers (≈ 40 % at cryogenic temperatures).¹⁰

Alloying can increase the technological potential of valleytronic TMDs by combining valley contrasting properties with band engineering.²³ Furthermore, alloys of structurally distinct TMDs may also enable phase change memory technologies²⁴⁻²⁶ by reducing the energy barrier between semiconducting and semimetallic states.²⁷ Few studies, however, have explored valley phenomena in alloys despite the heavy interest in this field. The first exploration of valley properties in alloys focused on $\text{Mo}_{1-x}\text{W}_x\text{Se}_2$ at 5 K and found that there was a transition from the intrinsic valley polarization of MoSe_2 to WSe_2 as the transition metal content was varied.²⁸ Experiments on a $\text{WS}_{0.6}\text{Se}_{1.4}$ alloy demonstrated a valley polarization of ≈ 31 % at 14 K, which was much lower than that of both WS_2 and WSe_2 .²⁹ A recent study of $\text{WS}_x\text{Te}_{2-x}$ found that the room temperature valley

polarization increased from 3 % in WS_2 to 37 % in an unspecified alloy composition.³⁰ The limited information regarding valley polarization in alloyed TMDs is a serious oversight as future valleytronics technologies will likely rely heavily on band engineering.

In this study, we examine the low-temperature optical properties of monolayer $\text{WSe}_{2(1-x)}\text{Te}_{2x}$, where the endpoints are the valleytronic semiconductor 1H- WSe_2 and the topological semimetal 1T_d - WTe_2 shown in **Figs. 1a** and **1b**. Prior studies of this alloy system were performed at 300 K and focused on unpolarized optical measurements³¹ as well as electronic transport characterization.³² Our study is unique in that it focuses on the impact of alloying on the valley excitons of $\text{WSe}_{2(1-x)}\text{Te}_{2x}$ monolayers encapsulated in hexagonal boron nitride (hBN) as shown in **Fig. 1c**. We ensure good interfacial contact in the heterostructure by cleaning with the nano-squeegee method,³³ which substantially improves the valley polarization. Raman measurements at 5 K show that increasing Te composition leads to the shifting and splitting of vibrational modes

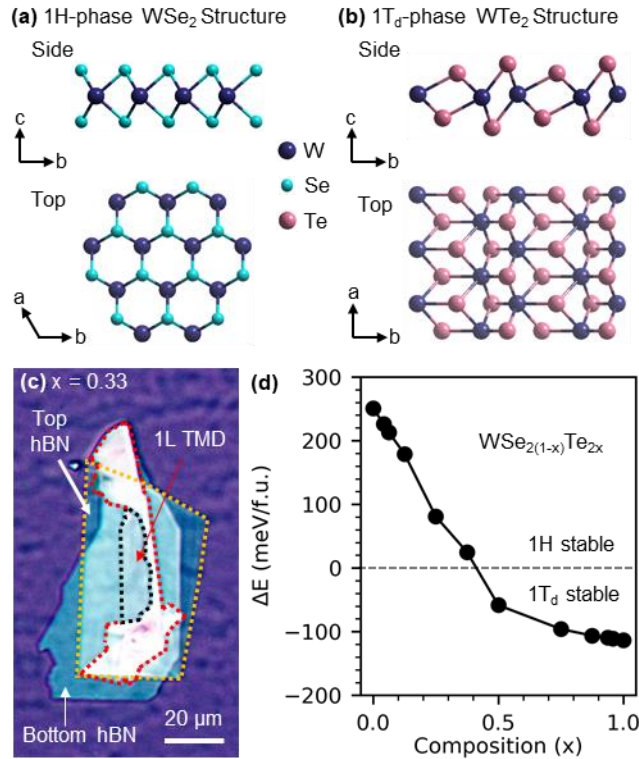


Fig. 1 | Structural phases and van der Waals heterostructures of $\text{WSe}_{2(1-x)}\text{Te}_{2x}$. Side and top view of (a) monolayer 1H- WSe_2 and (b) monolayer 1T_d - WTe_2 . (c) Optical image of an hBN-encapsulated $x = 0.33$ monolayer deposited onto a SiO_2/Si substrate. The TMD alloy is outlined in red and the monolayer (1L) portion of that flake is outlined in black. The top layer of hBN is outlined in yellow. (d) Composition-dependent phase diagram determined from DFT calculations indicating a phase boundary at $x = 0.4$.

as well as the appearance of new modes unique to alloys. Polarization-resolved Raman measurements coupled with density functional theory (DFT) calculations allow us to assign these alloy-only features as 1H-WTe₂ vibrational modes. Temperature-dependent, polarization-resolved PL measurements of the 1H-phase alloys demonstrate band gap tunability alongside the presence of new ultra-low energy emission features. We suggest these features are from deep mid-gap states that originate from the large difference in the W-Se and W-Te bond lengths. Despite the presence of structural disorder in the lattice, valley polarization is found to survive the alloying process for $x \leq 0.14$ while valley coherence is present for alloys $x \leq 0.37$, and interestingly we demonstrate that alloys have the ability to sustain these valley properties at higher temperatures than pure WSe₂. These findings illustrate the persistence of valley phenomena in significantly disordered alloys and point the way towards optimization of TMDs for novel phase change memories that naturally integrate with valleytronic devices.

Results

Stability and Vibrational Modes

Interpretation of our experimental data is guided by DFT modeling of the WSe_{2(1-x)}Te_{2x} phase diagram. Regarding crystal structure notation, we refer to T_d monolayers as being in the 1T_d phase. Previously, T_d and 1T' notations have been used interchangeably for T_d monolayers since the only difference between these structures in the bulk was believed to be a slight shift of layers relative to one another. Since the T_d structure contains three layers in its unit cell while the 1T' structure contains one layer, it was assumed that monolayers isolated from a bulk T_d crystal were in the 1T' phase. We make the 1T_d notation distinction in light of a recent report that has indicated, unlike the 1T' phase, inversion symmetry is broken in the monolayer T_d lattice.³⁴ We find from our DFT calculations, in agreement with previous studies,^{31,32} that the 1H phase is stable with a Te concentration of $x \leq 0.4$, which we illustrate in **Fig. 1d**. For $x \geq 0.5$, 1T_d becomes the lowest energy phase. As a result, we expect valleytronic optical properties for the 1H alloys corresponding to $x \leq 0.4$ and semimetallic behaviors for the 1T_d alloys $x \geq 0.5$. These predictions are consistent with our Raman and PL measurements described in detail below.

We first explore the effects of alloying on crystal structure through low-temperature Raman spectroscopy of hBN-encapsulated monolayer WSe_{2(1-x)}Te_{2x} shown in **Fig. 2a**. We fit this Raman

data with multiple Lorentzian peaks to extract mode frequencies, which are plotted in **Fig. 2b** with alloy composition x . It is instructive to examine the properties of the endpoints WSe_2 ($x = 0$) and

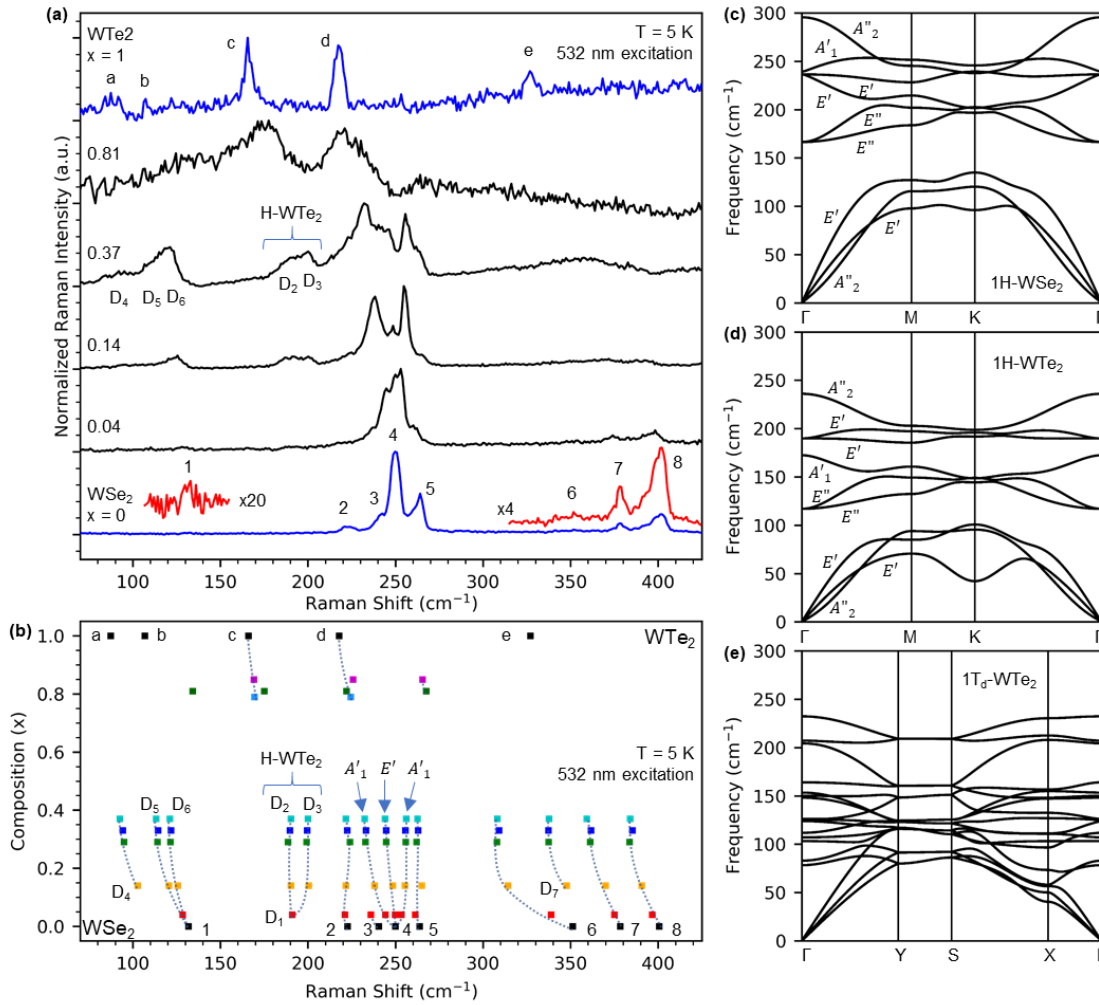


Fig. 2 | Composition-dependent Raman spectra of $\text{WSe}_{2(1-x)}\text{Te}_{2x}$ and phonon band structures of WSe_2 and WTe_2 . (a) Raman measurements of select $\text{WSe}_{2(1-x)}\text{Te}_{2x}$ alloys taken at 5 K with 532 nm excitation. Vibrational modes in pure WSe_2 and WTe_2 are identified with numbers and letters, respectively, and their assignments can be found in **Table 1**. Parts of the WSe_2 spectra are scaled for clarity. (b) Peak positions extracted from Raman measurements at 5 K for different alloy compositions x . Peaks identified in panel (a) for WSe_2 and WTe_2 are labeled with their respective numbers and letters. New alloy-induced vibrational modes are labeled D_i ($i = 1, 2, 3, \dots$). The shifting and the splitting of peaks are tracked with dotted lines. (c) Phonon band structure calculated for 1H- WSe_2 . (d) Phonon band structure calculated for 1H- WTe_2 . Peak D_1 is assigned to the 1H- WTe_2 A'_1 vibrational mode at 172 cm^{-1} , which splits with increasing x into peaks D_2 and D_3 . With low Te concentrations, the crystal remains globally in the 1H phase, thus permitting the presence of 1H- WTe_2 vibrational modes. (e) Phonon band structure calculated for 1T_d- WTe_2 .

WTe₂ ($x = 1$) that appear in blue in **Fig. 2a**. WSe₂, which naturally crystallizes in the 1H phase, is in the D_{3h} point group and exhibits modes with A'_1 and E' symmetries. In agreement with prior observations,^{35,36} we identify eight Raman peaks in WSe₂ at 132 cm⁻¹, 223 cm⁻¹, 240 cm⁻¹, 250 cm⁻¹, 264 cm⁻¹, 351 cm⁻¹, 378 cm⁻¹, and 401 cm⁻¹. These modes and their symmetries are summarized in **Table 1**. The dominant feature in the WSe₂ Raman spectra at 250 cm⁻¹ (labeled peak 4 in **Figs. 2a** and **2b**) is an A'_1 symmetry mode where the transition metal is fixed and the chalcogens vibrate perpendicular to the basal plane.^{37,38} In monolayer WSe₂, this mode overlaps with an E' symmetry mode where the chalcogen and transition metal layers both vibrate in-plane, but out of phase.^{37,38} These findings agree with prior calculations^{35,37,38} as well as our own DFT modeling of the WSe₂ phonon band structure that predicts the 0 K frequency of the dominant A'_1 mode at 239 cm⁻¹ and the E' mode at 236 cm⁻¹ (**Fig. 2c**). Additional monolayer WSe₂ modes are enhanced at 5 K, which are usually assigned as disorder-activated finite momentum phonons, combination modes, or difference modes.^{35,36,39} We find that previous assignments of these features to Raman difference modes conflict with our low-temperature data. Difference modes originate from a two-phonon process where one phonon is absorbed (anti-Stokes process) and another is created (Stokes process). Since this requires the presence of a phonon before photoexcitation, its occurrence is expected to follow a Boltzmann-like temperature dependence that disappears at cryogenic temperatures.⁴⁰ The presence of these so-called difference modes in our measurements at 5 K calls this assignment into question. Thus, it is more likely that these features are combination modes for which there are many possible assignments (**Table 1**), however there is presently no explanation for the mode at 132 cm⁻¹.

We present Raman data for bilayer WTe₂ to illustrate the stark differences between the 1T_d and 1H phases. The use of a bilayer flake does not adversely impact comparison to monolayer alloys since the Raman modes of greatest intensity are essentially identical in bilayer and monolayer WTe₂.⁴¹ This choice is further necessitated by the rapid oxidation of tellurium-based TMDs.⁴² Bilayer WTe₂ (T_d phase) belongs to the C_{2v} point group, and so only A_1 and A_2 symmetry modes can be observed.⁴³ Five peaks in the 70 - 425 cm⁻¹ range are present at 87 cm⁻¹, 107 cm⁻¹, 166 cm⁻¹, 218 cm⁻¹, and 327 cm⁻¹ and are labeled with letters in **Figs. 2a** and **2b**. Assignment of the mode symmetries is based on prior studies of WTe₂^{41,44} and are included in **Table 1**. The feature at 327 cm⁻¹, labeled peak e, has not been previously observed, and we assign it as either a second-order

overtone of the $166\text{ cm}^{-1} A_1$ mode (peak c) or a combination of the $107\text{ cm}^{-1} A_2$ and $218\text{ cm}^{-1} A_1$ modes (peaks b and d, respectively).

Low-temperature Raman measurements of the alloys (black curves of **Fig. 2a**) reveal fascinating new details regarding the vibrational modes that were not observed in Ref. 31 owing to thermal broadening at 300 K (see **Supplementary Fig. S1** for comparison of 5 K and 300 K spectra). Alloys with $x \leq 0.37$ are in the 1H phase and exhibit complex mode structures in the $\approx 230 - 275\text{ cm}^{-1}$ range. Polarization-resolved Raman measurements (**Supplementary Fig. S2**) reveal that the dominant $\text{WSe}_2 A'_1$ mode at 250 cm^{-1} exhibits two-mode behavior as it splits into two peaks at 244 cm^{-1} and 253 cm^{-1} for $x = 0.04$ (see red points in **Fig. 2b**). This differs from studies of $\text{WS}_{2(1-x)}\text{Se}_{2x}$ where this primary out-of-plane WSe_2 feature exhibited one-mode behavior with alloying.^{45,46} However, the splitting of out-of-plane vibrational modes with alloying has been seen in $\text{MoS}_x\text{Se}_{2-x}$ monolayers^{47,48} and has been carefully documented in few-layer $\text{MoS}_x\text{Se}_{2-x}$.⁴⁹ Jadczyk et al. attributed the splitting of this feature in alloys to the polarization of the alloy unit cell due to the substitution of heavier chalcogens that introduce different force constants in the lattice.⁴⁹ Thus,

1H-WSe₂		
Label	Position (cm ⁻¹)	Assignment
1	132	unknown
2	223	$E'(K)^a$
3	240	$E'(M)^a$
4	250	$A'_1 + E'$
5	264	$2LA(M)^{a,b}$
6	351	$2E'(\Gamma)^b$ or $A'_1(M) + TA(M)^b$
7	378	$[E'(\Gamma) \text{ or } A'_1(\Gamma)] + LA(M)^{a,b}$
8	401	$[E'(\Gamma) \text{ or } A'_1(\Gamma)] + LA(K)^a$ or $3LA(M)^{a,b}$

T_d-WTe₂ (bilayer)		
Label	Position (cm ⁻¹)	Assignment
a	87	A_2
b	107	A_2
c	166	A_1
d	218	A_1
e	327	$2A_1$ (2x peak c) or $A_1 + A_2$ (peak d + peak b)

Table 1. | Raman mode assignments. 1H-WSe₂ and T_d-WTe₂ (bilayer) vibrational mode symmetry assignments for the peaks identified in **Figs. 2a** and **2b**. WSe₂ peaks are labeled with numbers and WTe₂ peaks are labeled with letters. The superscripts a and b refer to assignments made in Refs. 35 and 36, respectively.

due to the splitting of the primary A'_1 mode, we find that the E' mode is distinguishable from the A'_1 mode in alloy monolayers and only slightly shifts to lower frequencies with increasing x .

Several other WSe_2 -like vibrational modes show sensitivity to alloying for 1H-phase compositions $x \leq 0.37$. Second-order finite momentum peaks 6, 7, and 8 of **Figs. 2a** and **2b** shift to lower frequencies and broaden with increasing alloy composition. This alloy data may clarify disagreements in the literature on whether A'_1 or E' phonons are the dominant contributor to these higher-order modes.^{35,36} The band predictions of 1H- WSe_2 in **Fig. 2c** show both branches of the E' mode that originate at 236 cm^{-1} shift to lower frequencies away from the Γ point. This behavior is opposite to that of the A'_1 mode, which originates at 239 cm^{-1} and shifts to higher frequencies away from the Γ point. Since peaks 6, 7, and 8 broaden asymmetrically on the lower frequency side of their centers as x is increased, this may indicate that the E' mode, rather than the A'_1 mode, contributes to these higher-order processes. The shifting and broadening of the WSe_2 modes for compositions $x \leq 0.37$ indicate that alloying introduces significant disorder into the lattice but globally maintains the 1H phase.

A particularly interesting alloy-induced feature resolved in 1H samples is the Raman peak labeled D_1 at 191 cm^{-1} in $x = 0.04$ (red points in **Fig. 2b**). This feature splits into the two peaks labeled D_2 and D_3 at 190 cm^{-1} and 200 cm^{-1} , respectively, as x is increased. Polarization-resolved Raman measurements (**Supplementary Fig. S2**) indicate that these features have A'_1 symmetry and DFT calculations of the 1H- WSe_2 phonon band structure (**Fig. 2c**) show no A'_1 phonon modes present in this range. We therefore calculate the phonon band structure of 1H- WTe_2 in **Fig. 2d**, which predicts an A'_1 Γ -point mode at 172 cm^{-1} . This mode is the closest to the observed results and so we tentatively assign the D_1 peak to the 1H- WTe_2 A'_1 mode and attribute its splitting to increasing force constant variations introduced into the lattice with high Te doping as discussed previously for the primary A'_1 mode of WSe_2 .⁴⁹ Raman measurements reveal several other new peaks in the 1H alloys, which we label D_4 , D_5 , D_6 , and D_7 in **Fig. 2b**. These polarization-independent features (see **Supplementary Fig. S2**) most likely arise from either finite momentum WSe_2 -like phonons or WSe_2 combination modes. We exclude difference modes based on the use of low-temperature spectroscopy as discussed previously. Possible assignments are $E'(M)$ for D_6 and $E' + E'(M)$ for D_7 , while D_4 and D_5 remain unassigned but may originate from combinations of 1H- WSe_2 and 1H- WTe_2 modes. As $WSe_{2(1-x)}Te_{2x}$ transitions to the $1T_d$ phase with alloying, the Raman spectra for x

≥ 0.79 show the two primary A_1 vibrational modes of pure WTe_2 , labeled peaks c and d in **Figs. 2a** and **2b**. These features are shifted and broadened due to alloy disorder in agreement with other WTe_2 alloys.⁵⁰

Excitonic Properties

In **Fig. 3**, we present temperature-dependent PL spectra for representative 1H-phase alloys. Each spectrum has been normalized by the maximum intensity and was excited with right circularly polarized light ($\sigma+$) at 1.96 eV. The collected PL is passed through a waveplate/analyzer combination to select $\sigma+$ emission. At 300 K, the PL spectra show contributions from both the neutral exciton (X^0) and the trion (X^T).¹³ Increasing the Te concentration causes both features to redshift due to the lower band gap of 1H- WTe_2 .⁵¹ As temperature decreases from 300 K to 5 K, X^0 and X^T sharpen, blueshift, and weaken in intensity. The latter behavior is due to the sign of the conduction band spin-orbit coupling, which makes the lowest exciton state dark (see the band schematic of WSe_2 in **Fig. 5a**).⁵² The sign of the spin-orbit coupling is the same for all W-based TMDs⁵² and so we expect no change in the optical activity of the lowest exciton state with Te substitution. The presence of broad features at lower energies compared to X^0 and X^T originate from a combination of higher-order excitonic complexes⁵³ and localized exciton states from lattice defects, strain, and residual impurities introduced during fabrication.^{10,13,54}

We explore band gap tunability of 1H- $\text{WSe}_{2(1-x)}\text{Te}_{2x}$ by extracting X^0 energy as a function of temperature, which is plotted in **Fig. 4a**. This data is fit with a semi-empirical formula for temperature-dependent optical band gaps given by⁵⁵

$$E_g(T) = E_0 - S\langle\hbar\omega\rangle \left[\coth\left(\frac{\langle\hbar\omega\rangle}{2kT}\right) - 1 \right], \quad (1)$$

where E_0 is the gap at absolute zero, S is a dimensionless electron-phonon coupling parameter, $\langle\hbar\omega\rangle$ is an average phonon energy, and k is the Boltzmann constant. This formula models the reduction in band gap with increasing temperature due to a combination of increasing lattice constants and exciton-phonon coupling.⁵⁵ Fits of our data to equation (1) are presented as solid lines in **Fig. 4a** and the compositional dependence of E_0 , S , and $\langle\hbar\omega\rangle$ from these fits are plotted in **Figs. 4b-d**. **Figure 4b** shows that E_0 (i.e. X^0 energy) varies in 1H- $\text{WSe}_{2(1-x)}\text{Te}_{2x}$ from ≈ 1.735 eV in WSe_2 to ≈ 1.519 eV in the $x = 0.37$ alloy. These experimental results agree extremely well with

the optical band gaps of the alloys computed using DFT with the HSE06 exchange-correlation functional,^{56,57} which predict a gap of 1.75 eV in 1H-phase WSe₂ that decreases to 1.53 eV at a Te concentration of $x = 0.375$ (blue triangles of **Fig. 4b**). At higher x the system transforms to the 1T_d phase (**Supplementary Fig. S3**) which is a semimetal. For a comparison of DFT results for the

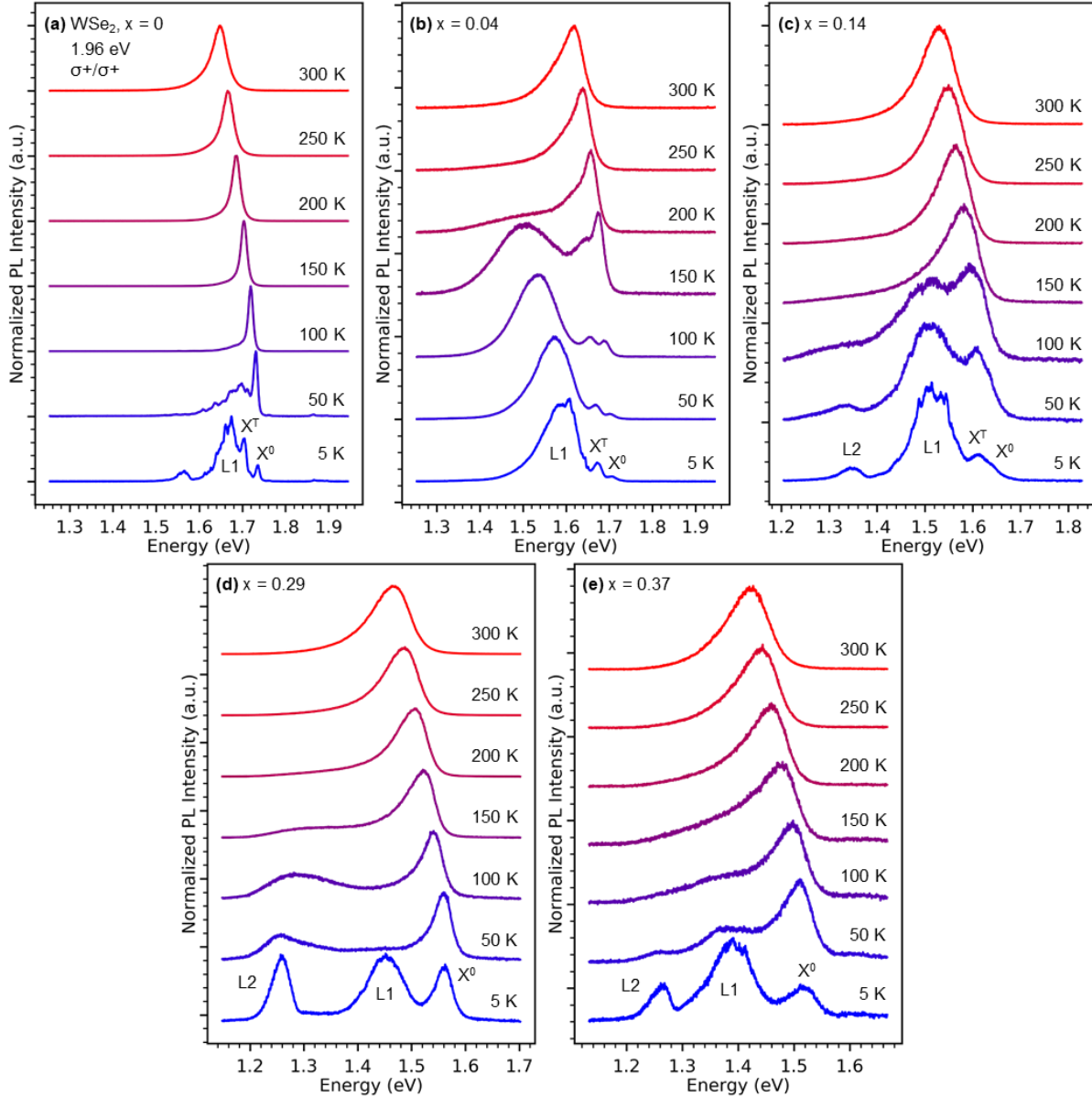


Fig. 3 | Temperature-dependent PL of 1H-WSe_{2(1-x)}Te_{2x}. PL measurements (1.96 eV excitation) of (a) WSe₂, as well as 1H-phase WSe_{2(1-x)}Te_{2x} alloys corresponding to (b) $x = 0.04$, (c) $x = 0.14$, (d) $x = 0.29$, and (e) $x = 0.37$. Excitation and collection are done with right circularly polarized light (σ^+). The neutral exciton (X^0) and trion (X^T) are labeled where appropriate. Emission at 300 K is dominated by X^0 , which has a low-energy tail resulting from the presence of X^T . As the temperature is decreased, X^0 and X^T sharpen and blueshift while the localized exciton features L1 and L2 begin to dominate the spectra.

optical band gaps of all $\text{WSe}_{2(1-x)}\text{Te}_{2x}$ monolayers calculated using both the HSE06 and PBE functionals and the density of states determined using the HSE06 functional, see **Supplementary Fig. S3**. Since the alloys are in the 1H phase only up to $x = 0.37$ and 1H-WTe₂ does not exist in nature, we are unable to reliably determine the bowing parameter for E_0 .²³ Therefore, we instead fit E_0 from $x = 0$ to 1 with a linear function as shown by the red line in **Fig. 4b**. From a linear extrapolation to $x = 1$, we determine the 0 K optical band gap of 1H-WTe₂ to be 1.15 eV. Lastly, extracted values for S range from 1.93 - 2.24 and for $\langle \hbar\omega \rangle$ between 4 - 16 meV (32.3 - 129 cm^{-1}), and are plotted versus x in **Figs. 4c** and **4d**.

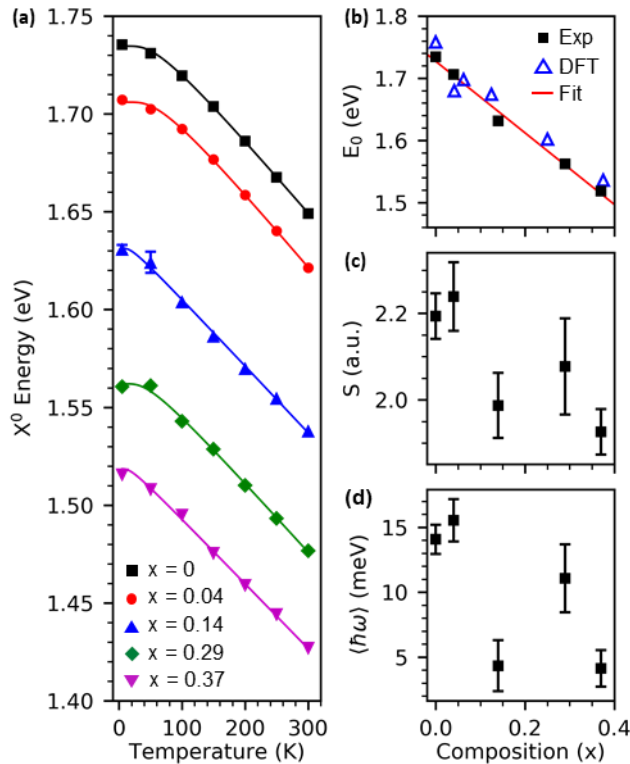


Fig. 4 | Composition- and temperature-dependent exciton energies. (a) X^0 energies extracted from temperature-dependent PL measurements (1.96 eV excitation). Excitation and collection are done with right circularly polarized light. The solid lines are fits to equation (1). The compositional dependence of the extracted parameters E_0 , S , and $\langle \hbar\omega \rangle$ are plotted in panels (b), (c), and (d), respectively. E_0 is found to be tunable with alloying, while S and $\langle \hbar\omega \rangle$ are found to decrease with increasing alloy composition x . In panel (b), we plot DFT predicted optical band gaps as blue triangles, while the red curve is a fit to a line used to extract a 0 K band gap for 1H-WTe₂ of 1.15 eV. 1σ error bars are shown in all panels.

Elaborating on the 5 K PL spectra of **Fig. 3**, we find that X^T appears ≈ 30 meV below X^0 in our data and shifts in lockstep with the neutral exciton so that there is only weak dependence of the X^0 - X^T binding energy on x (**Supplementary Fig. S4**). Spatial PL mapping of an $x = 0.33$ alloy

sample at 5 K indicates little variation of the intensities, energies, and linewidths of X^0 and X^T . These maps are discussed in detail in **Supplementary Note 1** and **Supplementary Fig. S5**. Additionally, we find evidence for excitonic transitions and exciton-phonon complexes at energies *above* X^0 known to originate from coupling between hBN and WSe₂ in van der Waals heterostructures.^{58,59} A detailed discussion of these features is presented in **Supplementary Note 2** and **Supplementary Fig. S6**. In 5 K and 300 K reflectance measurements presented in **Supplementary Fig. S7**, both the A and B excitons are clearly visible and the valence band spin-orbit coupling is found to increase with Te incorporation.

Localized excitons are common in W-based TMDs owing to the long lifetime of the dark exciton ground states. We identify such features in all alloys and the parent compound WSe₂, beginning with an emission band ≈ 100 meV below X^0 hereafter referred to as L1. For all $x > 0.04$, L1 is accompanied by a second localized emission feature (L2) approximately ≈ 300 meV below X^0 (**Figs. 3c-e**). This feature has never been observed in TMDs, alloyed or otherwise. L1 and L2 maintain a similar energy separation with respect to X^0 at all nonzero x but do exhibit variations in their temperature dependent behaviors.

The new defect band L2 must originate from a disorder unique to Te-rich alloys and may be connected to the preference of WTe₂ to crystallize in a 1T_d structure. Scanning tunneling electron microscopy measurements and molecular dynamics (MD) simulations of a similar alloy system, WS_{2-x}Te_x,⁶⁰ indicate that Te-substitution at levels approaching 15 % can substantially modify the structure of a 1H-phase alloy. The bond lengths and lattice constants of 1H-WSe₂ with 1H-WTe₂ are predicted to differ by $\approx 7 - 8$ %, ⁶⁰ which also leads to a mismatch between the metal-chalcogen bond angles. The MD simulations of Ref. 60 illustrate that these internal strains can lead to the displacement of Te atoms from the expected chalcogen site for concentrations as low as 8 %. These shifts lead to the compression and stretching of neighboring hexagonal rings, and in turn result in the displacement of the native chalcogen and even the W atoms. For the WS₂ – WTe₂ alloys studied in Ref. 60, continuing to increase the Te doping to 15 %, 20 %, and finally 25 % increased the displacements of W, S, and Te atoms, and ultimately drove the W atoms closer together in a prelude to the 1H - 1T_d transition. These Te concentrations compare favorably with the values at which we observe the presence of the L2 feature (**Fig. 3**). The presence of such substantial atomic displacements and internal strains seems to be unique to TMD alloys that are mixtures between

different structural phases. We therefore suggest that the internal strains driven by Te incorporation in 1H-phase alloys create a new band of defect states (i.e. the L2 feature) lower than those typically expected from chalcogen or transition metal vacancies (i.e. the L1 feature).⁵⁴

Valley Phenomena

Next, we explore valley contrasting in 1H-WSe_{2(1-x)}Te_{2x} alloys at 5 K using 1.96 eV excitation with σ^+ polarization. The schematic band structure in **Fig. 5a** illustrates the spin-valley polarized selection rules in WSe₂, where transitions between the valence band and the second highest conduction band are σ^+ (σ^-) polarized at the K (K') point. Any emission in the opposite polarization channel is a sign of intervalley scattering. Valley polarization is determined by measuring co- and cross-polarized PL spectra in the circular basis as shown in **Fig. 5b**. The degree of valley polarization ρ_{VP} for σ^+ excitation is defined as $\rho_{VP} = (I_{\sigma^+} - I_{\sigma^-}) / (I_{\sigma^+} + I_{\sigma^-})$, where I_{σ^+} (I_{σ^-}) is the intensity of the collected light with σ^+ (σ^-) orientation. Valley coherence measurements are similar except measurements are carried out in a linear basis with co-polarized (\parallel) and cross-polarized (\perp) configurations as shown in **Fig. 5c**. The degree of valley coherence ρ_{VC} is calculated similarly as $\rho_{VC} = (I_{\parallel} - I_{\perp}) / (I_{\parallel} + I_{\perp})$, where I_{\parallel} (I_{\perp}) is the intensity of the collected light that is \parallel (\perp) to the incident light.

Alloy-dependent values of ρ_{VP} for X^0 (black squares) and X^T (red circles) at 5 K are plotted in **Fig. 5d**. We find that $\rho_{VP} \approx 49\%$ for X^0 in WSe₂, which agrees with previously reported values.¹⁰ Achieving this value required cleaning our heterostructures post-assembly using the nano-squeegee technique.³³ This process improved the WSe₂ ρ_{VP} of X^0 by a factor of ≈ 1.7 , thus increasing the signal from 29% to 49%, whereas it appeared to have very little effect on ρ_{VC} . This result illustrates the impact of contaminants on valley properties and a comparison of squeegeed and non-squeegeed alloys can be found in **Supplementary Fig. S8**.

As Te is substituted into the lattice, ρ_{VP} first remains unchanged at $x = 0.04$ and then decreases to 32% at $x = 0.14$ (**Fig. 5d**). For $x > 0.14$, no valley polarization is observed. The trion exhibits a similar trend with x ; $\rho_{VP} \approx 67\%$ for X^T in WSe₂ and is zero for $x > 0.14$. To the best of our knowledge, there is no systematic theory for understanding valley depolarization from alloy disorder. However, we do observe an interesting correlation between ρ_{VP} and the intensity ratio of

X^T / X^0 , which decreases from ≈ 3 to ≈ 0.25 with Te incorporation (**Supplementary Fig. S9**). This suggests a connection between ρ_{VP} and an apparent reduction in doping with increasing Te

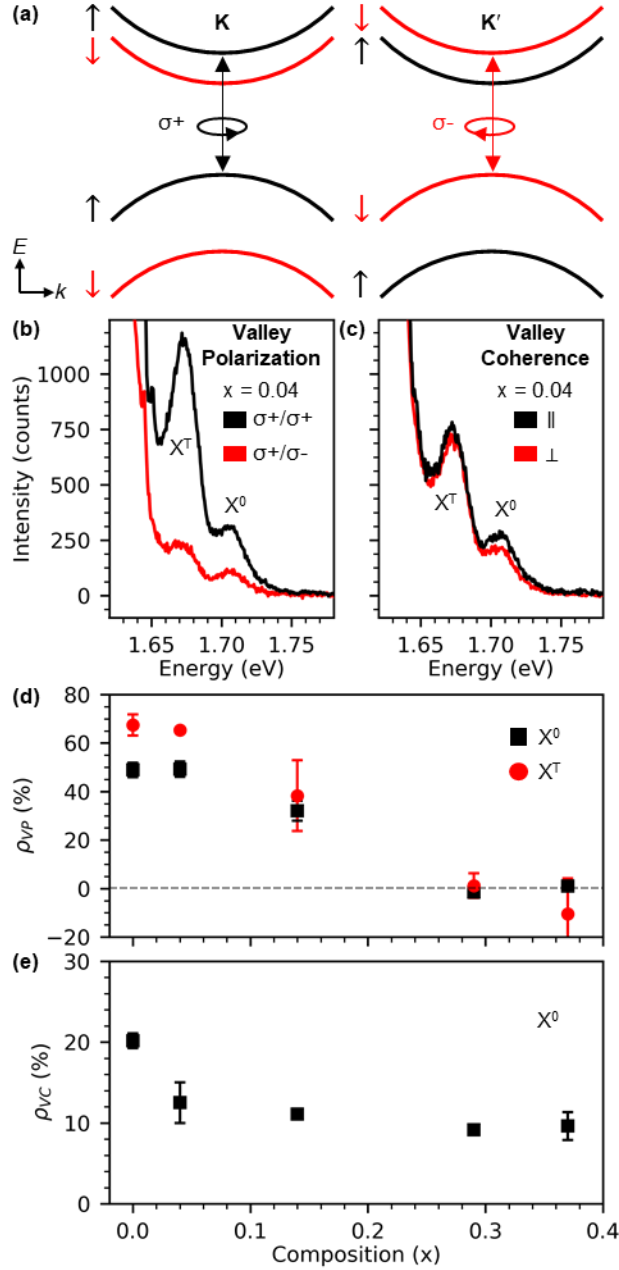


Fig. 5 | Valley properties of $\text{WSe}_{2(1-x)}\text{Te}_{2x}$ at 5 K. (a) Simplified image of the electron bands near the K and K' points of the hexagonal Brillouin zone in monolayer WSe_2 . Valley-dependent optical selection rules couple transitions at the K (K') valleys with $\sigma+$ ($\sigma-$) circularly polarized light. (b) and (c) show example spectra of valley polarization and valley coherence measurements for $x = 0.04$, respectively. (d) The degree of valley polarization (ρ_{VP}) of X^0 (black squares) and X^T (red circles) and (e) the degree of valley coherence (ρ_{VC}) of X^0 plotted against alloy composition x . 1σ error bars are shown in panels (d) and (e).

substitution. Valley coherence is only present for neutral excitons¹⁰ and we plot ρ_{VC} versus x at 5 K in **Fig. 5e**. $\rho_{VC} \approx 20\%$ in WSe₂, which is slightly lower than the literature value,¹⁰ and decreases to $\approx 13\%$ when $x = 0.04$ after which point it remains essentially constant until the 1H-1T_d phase transition. We note that valley coherence remains finite even when valley polarization goes to zero at large x .

ρ_{VP} and ρ_{VC} are found to monotonically decrease with temperature (**Fig. 6** and **Supplementary Fig. S10**, respectively) for all alloy compositions, but at different rates in each case. In WSe₂, our results for $\rho_{VP}(T)$ are consistent with other studies of monolayer WSe₂.^{13,61} The origin of valley depolarization in TMDs remains a hotly debated topic. The prevailing theories regarding valley dynamics indicate that electron-hole exchange,^{9,19} intervalley phonon scattering,^{8,20} and Coulomb screening⁶² of the exchange interaction all substantially impact the valley lifetime. In the recent work of Ref. 21, the authors present experimental evidence for a mechanism where momentum-dependent electron-hole exchange interactions drive valley depolarization and can be screened by the ‘intrinsic’ doping commonly occurring in TMDs.²¹ The importance of carrier doping is highlighted by a later study where doping was used to engineer valley polarization over a wide range of temperatures.²² The presence of defects in our 1H-phase alloys complicates this picture as they effectively shorten the X^0 lifetime, which can in turn enhance valley polarization by accelerating recombination.⁶³ However, the versatility of the formalism in Ref. 21 makes it potentially useful for modeling our data even though our alloys are far from the ideal case. The temperature dependence of the valley polarization can be expressed as²¹

$$\rho_{VP}(T) = \frac{\rho_{VP_0}}{1 + \frac{A}{\hbar[1 - \exp(-E_F/kT)]^2}}, \quad (2)$$

where k is the Boltzmann constant, ρ_{VP_0} is initial valley polarization upon photoexcitation, and A is a material-dependent constant proportional to the product of the average exciton lifetime and the exciton linewidth. The parameter E_F is the Fermi energy measured from the bottom of the conduction band or the valence band, depending on the sign of the doping, and accounts for the effect of carrier screening of the intervalley exchange interaction. As temperature increases, carriers in the dopant/defect states near the conduction band are ionized and screening of the intervalley exchange interaction becomes less effective, resulting in a concomitant drop in ρ_{VP} . All parameters in equation (2) are allowed to vary during the fit and the resulting values of E_F are

inset in **Fig. 6**. The slight decrease in E_F with x suggests that alloying generates a higher carrier density and could be responsible for the larger temperature plateau in **Fig. 6**. However, this is somewhat at odds with our observation of the X^T / X^0 intensity ratio where large x samples have a smaller X^T component (**Supplementary Fig. S9**). It may be the case that Te doping does introduce new carriers into the system for screening, but also dopes the material in an unexpected way. While the fit of equation (2) is compelling, we caution in extracting too much physical meaning from it. The formalism is designed to be versatile and applied to atomically flat monolayer TMDs. However, recent DFT and scanning transmission electron microscopy evidence⁶⁰ suggests that suitably high Te doping leads to out-of-plane structural distortions of TMDs. This new kind of defect likely affects valley polarization, but the exact mechanism is currently unknown.

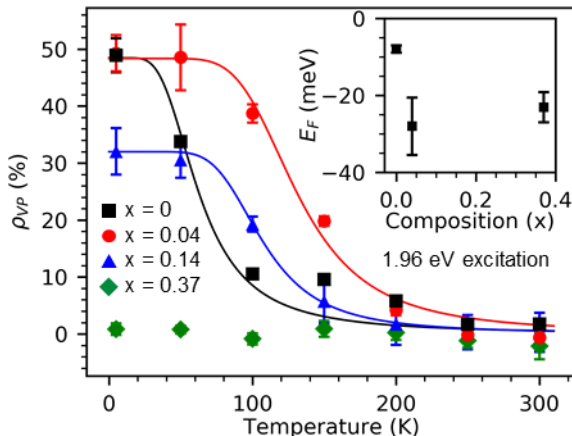


Fig. 6 | Temperature dependence of ρ_{VP} in $1H-WSe_{2(1-x)}Te_{2x}$. Measurements are done using 1.96 eV excitation. Solid lines are fits to equation (2) from the text for steady-state exciton valley polarization. The $x = 0.04$ and $x = 0.14$ alloys are found to sustain valley properties at elevated temperatures and are less susceptible to phonon-induced valley depolarization when compared to pure WSe_2 ($x = 0$). The inset shows the alloy dependence of E_F extracted from the fits. 1σ error bars are shown in all panels.

Discussion

We have used low-temperature Raman and temperature-dependent, polarization-resolved PL spectroscopy to characterize different crystal phases spanned by monolayer $WSe_{2(1-x)}Te_{2x}$ alloys and explore how incorporation of Te into the lattice affects valleytronic and semiconducting properties. DFT calculations of the phonon dispersion curves for $1H-WSe_2$ and $1T_d-WTe_2$ alongside low-temperature Raman measurements allowed us to assign the vibrational modes of the WSe_2 and WTe_2 endpoint compounds. The shifting and splitting of these vibrational modes

were tracked with alloy composition x , and we found the activation of alloy-only features that we assigned to 1H-WTe₂ vibrational modes using DFT calculations of the 1H-WTe₂ phonon dispersion curves and polarization-resolved Raman measurements. Temperature-dependent PL measurements were used to identify excitonic transitions, exciton-phonon coupling features, and new defect-related emission, as well as demonstrate band gap tunability. DFT calculations of the optical band gap in the alloys agreed very well with experiment when using the HSE06 functional. Polarization-resolved PL measurements showed that not only does the valley polarization of X^0 and X^T and the valley coherence of X^0 survive the alloying process, but valley coherence is present for higher alloy concentrations than ρ_{VP} . Additionally, we found that the valley polarization of X^0 is sustained at higher temperatures than pure WSe₂. Reflectance measurements were also used to measure the A and B excitons in select alloys, indicating that the spin-orbit splitting of the valence band can be tuned with alloying. This study illustrates the resilience of valley phenomena in alloys and demonstrates the potential for optimizing the semiconducting and valley properties of 2D TMDs for phase change memory and valleytronic applications.

Methods

WSe_{2(1-x)}Te_{2x} alloys ($x = 0 \dots 1$) were grown by the chemical vapor transport (CVT) method. Appropriate amounts of W (99.9 %), Se (99.99 %), and Te (99.9 %) powders were loaded in quartz ampoules together with ≈ 90 mg (≈ 4 mg per cm³ of the ampoule's volume) of TeCl₄ which served as a transport agent. The ampoules were then sealed under vacuum and slowly heated in a single-zone furnace until the temperature at the source and the growth zones reached 980 °C and 830 °C, respectively. After 4 days of growth, the ampoules were ice-water quenched. Crystal phases of the alloys were determined by examining powder X-ray diffraction patterns using MDI-JADE 6.5 software package.* We found that alloys with $x \leq 0.4$ crystallized in the 2H phase and those with $x \geq 0.8$ were in the T_d phase. Results are consistent with the reports of Ref. 31. Chemical compositions were determined by the energy-dispersive X-ray spectroscopy (EDS) using a JEOL JSM-7100F field-emission scanning electron microscope (FESEM) equipped with an Oxford Instruments X-Max 80 EDS detector.

For optical studies, WSe_{2(1-x)}Te_{2x} bulk crystals were mechanically exfoliated and monolayers were identified by optical contrast. Monolayers were then fully encapsulated in an hBN heterostructure

(top and bottom layer) using the viscoelastic dry-stamping method on a SiO₂/Si substrate (90 nm oxide thickness) to protect them from the degradative effects due to exposure to the atmosphere and to provide a uniform dielectric environment.⁶⁴ We note that before encapsulation, monolayers were exposed to the atmosphere for less than one hour. To guarantee clean hBN/TMD contact, the nano-squeegee method was used with a scan line density of ≥ 10 nm/line and a scan speed of ≤ 30 $\mu\text{m/s}$ as suggested by Rosenberger et al. to physically push contaminants out from in between heterostructure interfaces.³³ Results of this procedure can be seen in the atomic force microscope image of **Supplementary Fig. S5**. Here, the contaminants removed from the interfaces are gathered along both sides of the nano-squeegeed region (dark vertical lines, ≈ 50 nm in height above sample).

Raman and PL measurements were performed on home-built confocal microscopes, both in backscattering geometries, that were integrated with a single close-cycle cryostat (Montana Instruments Corporation, Bozeman, MT). The excitation source for Raman measurements was a 532 nm laser, while the excitation source for PL measurements was a 633 nm laser. Both setups focus the excitation source through a 0.42 NA long working distance objective with 50X magnification. For Raman measurements, the laser spot was ≈ 2.4 μm , and the laser power density was fixed at $66 \mu\text{W}/\mu\text{m}^2$, while for PL measurements, the laser spot was determined to be ≈ 2.2 μm , and the laser power density was fixed at $21 \mu\text{W}/\mu\text{m}^2$. Collected light in both cases was directed to a 500 nm focal length spectrometer with a liquid nitrogen-cooled CCD (Princeton Instruments, Trenton, NJ). The spectrometer and camera were calibrated using a Hg-Ar atomic line source. For spectral analysis, Raman peaks were fit with Lorentzian profiles, whereas PL peaks were fit with Gaussians.

Density functional theory calculations were performed using the Vienna *ab initio* Simulation Package (VASP).^{65–67} Projector augmented wave (PAW) pseudopotentials⁶⁸ and the PBE exchange-correlation functional⁵⁶ were utilized. Spin-orbit coupling was included in all calculations except for the phonon band structure, which is a standard procedure.⁶⁹ It has been recently reported that there are slight differences between the 1T' and 1T_d phases in monolayer TMDs,³⁴ with WTe₂ likely forming in the 1T_d phase. However, in this work we performed all calculations with the WTe₂ monolayer in the 1T' structure. Owing to very small differences between the 1T' phase and 1T_d phase, this assumption is appropriate. Full relaxations of the lattice

parameters and ionic positions were performed on monolayer WSe₂ and WTe₂ in the 1H and 1T' phases using a 32×32×1 and 32×16×1 Γ -centered k-mesh, respectively, and a 500 eV plane-wave cutoff. The phonon band structures of these compounds were computed using density functional perturbation theory (DFPT).⁷⁰ Various chalcogen-alloyed compositions of the form WSe_{2(1-x)}Te_{2x} were created by expanding these unit cells and substituting the appropriate amount of Te with Se (or vice-versa). Full relaxations were again performed in each case, with the k-mesh scaled appropriately to the size of the unit cell. In the case when multiple substitutional anions were needed to achieve a given composition, all combinations of the position of the alloying atoms relative to each other were tested, with the lowest energy configuration considered the ground state (**Supplementary Fig. S11**). The density of states was computed using the aforementioned PBE functional, as well as the HSE06 functional,⁵⁷ with 25 % Hartree-Fock exact exchange included.

References

1. Vitale, S. A. *et al.* Valleytronics: Opportunities, Challenges, and Paths Forward. *Small* **14**, 1801483 (2018).
2. Xu, X., Yao, W., Xiao, D. & Heinz, T. F. Spin and pseudospins in layered transition metal dichalcogenides. *Nat. Phys.* **10**, 343–350 (2014).
3. Mak, K. F., Xiao, D. & Shan, J. Light–valley interactions in 2D semiconductors. *Nat. Photonics* **12**, 451–460 (2018).
4. Schaibley, J. R. *et al.* Valleytronics in 2D materials. *Nat. Rev. Mater.* **1**, (2016).
5. Žutić, I., Fabian, J. & Das Sarma, S. Spintronics: Fundamentals and applications. *Rev. Mod. Phys.* **76**, 323–410 (2004).
6. Splendiani, A. *et al.* Emerging Photoluminescence in Monolayer MoS₂. *Nano Lett.* **10**, 1271–1275 (2010).
7. Mak, K. F., Lee, C., Hone, J., Shan, J. & Heinz, T. F. Atomically Thin MoS₂: A New Direct-Gap Semiconductor. *Phys. Rev. Lett.* **105**, 136805 (2010).
8. Zeng, H., Dai, J., Yao, W., Xiao, D. & Cui, X. Valley polarization in MoS₂ monolayers by optical pumping. *Nat. Nanotechnol.* **7**, 490–493 (2012).
9. Mak, K. F., He, K., Shan, J. & Heinz, T. F. Control of valley polarization in monolayer MoS₂ by optical helicity. *Nat. Nanotechnol.* **7**, 494–498 (2012).
10. Jones, A. M. *et al.* Optical generation of excitonic valley coherence in monolayer WSe₂. *Nat. Nanotechnol.* **8**, 634–638 (2013).
11. Wang, G. *et al.* Valley dynamics probed through charged and neutral exciton emission in monolayer WSe₂. *Phys. Rev. B* **90**, 075413 (2014).
12. Hao, K. *et al.* Direct measurement of exciton valley coherence in monolayer WSe₂. *Nat. Phys.* **12**, 677–682 (2016).

13. Huang, J., Hoang, T. B. & Mikkelsen, M. H. Probing the origin of excitonic states in monolayer WSe₂. *Sci. Rep.* **6**, 22414 (2016).
14. Wang, G. *et al.* Control of Exciton Valley Coherence in Transition Metal Dichalcogenide Monolayers. *Phys. Rev. Lett.* **117**, 187401 (2016).
15. Aivazian, G. *et al.* Magnetic control of valley pseudospin in monolayer WSe₂. *Nat. Phys.* **11**, 148–152 (2015).
16. Chen, S.-Y. *et al.* Superior Valley Polarization and Coherence of 2s Excitons in Monolayer WSe₂. *Phys. Rev. Lett.* **120**, 046402 (2018).
17. Ye, Z., Sun, D. & Heinz, T. F. Optical manipulation of valley pseudospin. *Nat. Phys.* **13**, 26–29 (2016).
18. Tatsumi, Y., Ghalamkari, K. & Saito, R. Laser energy dependence of valley polarization in transition-metal dichalcogenides. *Phys. Rev. B* **235408**, 1–10 (2016).
19. Yu, T. & Wu, M. W. Valley depolarization due to intervalley and intravalley electron-hole exchange interactions in monolayer MoS₂. *Phys. Rev. B* **89**, 205303 (2014).
20. Kioseoglou, G. *et al.* Valley polarization and intervalley scattering in monolayer MoS₂. *Appl. Phys. Lett.* **101**, 221907 (2012).
21. Miyauchi, Y. *et al.* Evidence for line width and carrier screening effects on excitonic valley relaxation in 2D semiconductors. *Nat. Commun.* **9**, 1–10 (2018).
22. Shinokita, K. *et al.* Continuous Control and Enhancement of Excitonic Valley Polarization in Monolayer WSe₂ by Electrostatic Doping. *Adv. Funct. Mater.* **1900260**, 1–8 (2019).
23. Xie, L. M. Two-dimensional transition metal dichalcogenide alloys: Preparation, characterization and applications. *Nanoscale* **7**, 18392–18401 (2015).
24. Duerloo, K.-A. N., Li, Y. & Reed, E. J. Structural phase transitions in two-dimensional Mo- and W-dichalcogenide monolayers. *Nat. Commun.* **5**, 4214 (2014).
25. Rehn, D. A., Li, Y., Pop, E. & Reed, E. J. Theoretical potential for low energy consumption phase change memory utilizing electrostatically-induced structural phase transitions in 2D materials. *npj Comput. Mater.* **4**, 2 (2018).
26. Wang, X. *et al.* Potential 2D Materials with Phase Transitions: Structure, Synthesis, and Device Applications. *Adv. Mater.* **1804682**, 1804682 (2018).
27. Duerloo, K.-A. N. & Reed, E. J. Structural Phase Transitions by Design in Monolayer Alloys. *ACS Nano* **10**, 289–297 (2016).
28. Wang, G. *et al.* Spin-orbit engineering in transition metal dichalcogenide alloy monolayers. *Nat. Commun.* **6**, 10110 (2015).
29. Meng, Y. *et al.* Excitonic Complexes and Emerging Interlayer Electron–Phonon Coupling in BN Encapsulated Monolayer Semiconductor Alloy: WS_{0.6}Se_{1.4}. *Nano Lett.* **19**, 299–307 (2019).
30. Yun, S. J. *et al.* Telluriding monolayer MoS₂ and WS₂ via alkali metal sinter. *Nat. Commun.* **8**, 2163 (2017).
31. Yu, P. *et al.* Metal-Semiconductor Phase-Transition in WSe₂(1-x)Te_{2x} Monolayer. *Adv. Mater.* **29**, 1603991 (2017).

32. Lin, J. *et al.* Anisotropic Ordering in 1T' Molybdenum and Tungsten Ditelluride Layers Alloyed with Sulfur and Selenium. *ACS Nano* **12**, 894–901 (2018).
33. Rosenberger, M. R. *et al.* Nano-“Squeegee” for the Creation of Clean 2D Material Interfaces. *ACS Appl. Mater. Interfaces* **10**, 10379–10387 (2018).
34. Xu, S. Y. *et al.* Electrically switchable Berry curvature dipole in the monolayer topological insulator WTe₂. *Nat. Phys.* **14**, 900–906 (2018).
35. del Corro, E. *et al.* Excited Excitonic States in 1L, 2L, 3L, and Bulk WSe₂ Observed by Resonant Raman Spectroscopy. *ACS Nano* **8**, 9629–9635 (2014).
36. Zhao, W. *et al.* Lattice dynamics in mono- and few-layer sheets of WS₂ and WSe₂. *Nanoscale* **5**, 9677 (2013).
37. Terrones, H. *et al.* New First Order Raman-active Modes in Few Layered Transition Metal Dichalcogenides. *Sci. Rep.* **4**, 4215 (2015).
38. Luo, X. *et al.* Effects of lower symmetry and dimensionality on Raman spectra in two-dimensional WSe₂. *Phys. Rev. B - Condens. Matter Mater. Phys.* **88**, 1–7 (2013).
39. Sun, H. *et al.* Enhanced exciton emission behavior and tunable band gap of ternary W(S_xSe_{1-x})₂ monolayer: temperature dependent optical evidence and first-principles calculations. *Nanoscale* **10**, 11553–11563 (2018).
40. Cuscó, R. *et al.* Temperature dependence of Raman scattering in ZnO. *Phys. Rev. B* **75**, 165202 (2007).
41. Jiang, Y. C., Gao, J. & Wang, L. Raman fingerprint for semi-metal WTe₂ evolving from bulk to monolayer. *Sci. Rep.* **6**, 19624 (2016).
42. Ye, F. *et al.* Environmental Instability and Degradation of Single- and Few-Layer WTe₂ Nanosheets in Ambient Conditions. *Small* **12**, 5802–5808 (2016).
43. Cao, Y. *et al.* Anomalous vibrational modes in few layer WTe₂ revealed by polarized Raman scattering and first-principles calculations. *2D Mater.* **4**, 035024 (2017).
44. Kim, Y. *et al.* Anomalous Raman scattering and lattice dynamics in mono- and few-layer WTe₂. *Nanoscale* **8**, 2309–2316 (2016).
45. Duan, X. *et al.* Synthesis of WS₂xSe_{2-2x} Alloy Nanosheets with Composition-Tunable Electronic Properties. *Nano Lett.* **16**, 264–269 (2016).
46. Fu, Q. *et al.* Synthesis and Enhanced Electrochemical Catalytic Performance of Monolayer WS₂(1-x)Se_{2x} with a Tunable Band Gap. *Adv. Mater.* **27**, 4732–4738 (2015).
47. Mann, J. *et al.* 2-Dimensional Transition Metal Dichalcogenides with Tunable Direct Band Gaps: MoS₂(1-x)Se_{2x} Monolayers. *Adv. Mater.* **26**, 1399–1404 (2014).
48. Feng, Q. *et al.* Growth of MoS₂(1-x)Se_{2x} (x = 0.41–1.00) Monolayer Alloys with Controlled Morphology by Physical Vapor Deposition. *ACS Nano* **9**, 7450–7455 (2015).
49. Jadczyk, J. *et al.* Composition dependent lattice dynamics in MoS_xSe_(2-x) alloys. *J. Appl. Phys.* **116**, (2014).
50. Oliver, S. M. *et al.* The structural phases and vibrational properties of Mo_{1-x}W_xTe₂ alloys. *2D Mater.* **4**, 045008 (2017).

51. Kang, J., Tongay, S., Zhou, J., Li, J. & Wu, J. Band offsets and heterostructures of two-dimensional semiconductors. *Appl. Phys. Lett.* **102**, (2013).
52. Echeverry, J. P., Urbaszek, B., Amand, T., Marie, X. & Gerber, I. C. Splitting between bright and dark excitons in transition metal dichalcogenide monolayers. *Phys. Rev. B* **93**, 1–5 (2016).
53. Paur, M. *et al.* Electroluminescence from multi-particle exciton complexes in transition metal dichalcogenide semiconductors. *Nat. Commun.* **10**, 1709 (2019).
54. Tongay, S. *et al.* Defects activated photoluminescence in two-dimensional semiconductors: interplay between bound, charged and free excitons. *Sci. Rep.* **3**, 2657 (2013).
55. O'Donnell, K. P. & Chen, X. Temperature dependence of semiconductor band gaps. *Appl. Phys. Lett.* **58**, 2924–2926 (1991).
56. Perdew, J. P., Burke, K. & Ernzerhof, M. Generalized Gradient Approximation Made Simple. *Phys. Rev. Lett.* **77**, 3865–3868 (1996).
57. Heyd, J., Scuseria, G. E. & Ernzerhof, M. Hybrid functionals based on a screened Coulomb potential. *J. Chem. Phys.* **118**, 8207–8215 (2003).
58. Jin, C. *et al.* Interlayer electron–phonon coupling in WSe₂/hBN heterostructures. *Nat. Phys.* **13**, 127–131 (2017).
59. Chow, C. M. *et al.* Unusual Exciton–Phonon Interactions at van der Waals Engineered Interfaces. *Nano Lett.* **17**, 1194–1199 (2017).
60. Tang, B. *et al.* Phase-Controlled Synthesis of Monolayer Ternary Telluride with a Random Local Displacement of Tellurium Atoms. *Adv. Mater.* **1900862**, 1900862 (2019).
61. Hanbicki, A. T. *et al.* Optical polarization of excitons and trions under continuous and pulsed excitation in single layers of WSe₂. *Nanoscale* **9**, 17422–17428 (2017).
62. Konabe, S. Screening effects due to carrier doping on valley relaxation in transition metal dichalcogenide monolayers. *Appl. Phys. Lett.* **109**, 073104 (2016).
63. McCreary, K. M., Currie, M., Hanbicki, A. T., Chuang, H. J. & Jonker, B. T. Understanding Variations in Circularly Polarized Photoluminescence in Monolayer Transition Metal Dichalcogenides. *ACS Nano* **11**, 7988–7994 (2017).
64. Castellanos-Gomez, A. *et al.* Deterministic transfer of two-dimensional materials by all-dry viscoelastic stamping. *2D Mater.* **1**, 011002 (2014).
65. Kresse, G. & Furthmüller, J. Efficiency of ab-initio total energy calculations for metals and semiconductors using a plane-wave basis set. *Comput. Mater. Sci.* **6**, 15–50 (1996).
66. Kresse, G. & Furthmüller, J. Efficient iterative schemes for ab initio total-energy calculations using a plane-wave basis set. *Phys. Rev. B - Condens. Matter Mater. Phys.* **54**, 11169–11186 (1996).
67. Kohn, W. & Sham, L. J. Self-Consistent Equations Including Exchange and Correlation Effects. *Phys. Rev.* **140**, A1133–A1138 (1965).
68. P.E., B. Projector augmented-wave method. *Phys. Rev. B* **50**, 17953–17979 (1994).
69. Xiang, H. *et al.* Quantum spin Hall insulator phase in monolayer WTe₂ by uniaxial strain. *AIP Adv.* **6**, 095005 (2016).

70. Baroni, S., Giannozzi, P. & Testa, A. Green's-function approach to linear response in solids. *Phys. Rev. Lett.* **58**, 1861–1864 (1987).

Acknowledgements

P.M.V. and S.M.O. acknowledge support from the National Science Foundation (NSF) under Grant No. DMR-1748650, the George Mason University Quantum Materials Center, and the George Mason University Presidential Scholars Program. J.Y. was supported by funds from Binghamton University. Computational resources were provided by the Department of Defense High Performance Computing Modernization Program. S.K. acknowledges support from the US Department of Commerce, NIST under financial assistance award 70NANB18H155. T.L.R. was supported by the Office of Naval Research.

***Disclaimer:** Certain commercial equipment, instruments, or materials are identified in this paper in order to specify the experimental procedure adequately. Such identification is not intended to imply recommendation or endorsement by the National Institute of Standards and Technology, nor is it intended to imply that the materials or equipment identified are necessarily the best available for the purpose.

Author Contributions

P.M.V. and S.M.O. conceived and designed the experiments and wrote the manuscript with input from all coauthors. S.M.O. prepared van der Waals heterostructures and carried out all experiments. A.D.V. and S.K. grew the bulk crystals used in this work. J.Y. and T.L.R. performed the density functional theory calculations.

Competing Interests

The authors declare no competing financial interests.